Theoretical and Experimental Studies of Gallate Melilite Electrides From Topotactic Reduction of Interstitial Oxide Ions

Lijia Zhou, Jinxiao Zhang, Congling Yin, Luhui Meng, Jiachen Li, Yuexiang Li, Franck Fayon, Mathieu Allix, Xiaojun Kuang

Theoretical and Experimental Studies of Gallate Melilite Electrides from Topotactic Reduction of Interstitial Oxide Ion Conductor

Lijia Zhou[#, 1], Jinxiao Zhang[#, 2], Congling Yin[1], Luhui Meng[3], Jiachen Li,[1] Yuexiang Li[3], Franck Fayon[4], Mathieu Allix[4], Xiaojun Kuang[1,2]*

1. MOE Key Laboratory of New Processing Technology for Nonferrous Metal and Materials, Guangxi Key Laboratory of Optic and Electronic Materials and Devices, College of Materials Science and Engineering, Guilin University of Technology, Guilin 541004, PR China

2. Guangxi Key Laboratory of Electrochemical and Magneto-chemical Functional Materials, College of Chemistry and Bioengineering, Guilin University of Technology, Guilin 541004, P. R. China

3. Department of Chemistry, Nanchang University, Nanchang 330031, P. R. China

4. CNRS, CEMHTI UPR3079, Univ. Orléans, F-45071 Orléans, France

# These authors equally contribute to the manuscript.

* E-mail:kuangxj@glut.edu.cn

Abstract

Non-stoichiometric $La_{1.5}Sr_{0.5}Ga_3O_{7.25}$ melilite oxide ion conductor features active interstitial oxygen defects in the pentagonal rings with high mobility. In this study, electron localization function calculation by density functional theory indicated that the interstitial oxide ions located in the pentagonal rings of the gallate melilites may be removed and replaced by electron anions, which are confined within the pentagonal rings, which would therefore convert the melilite interstitial oxide ion conductor into a zero-dimensional (0D) electride. The more active interstitials oxide ions, compared to the framework oxide ions, make the $La_{1.5}Sr_{0.5}Ga_3O_{7.25}$ melilite structure more reducible by CaH_2 using topotactic reduction, in contrast with the hardly reducible nature of the parent $LaSrGa_3O_7$. The topotactic reduction enhances the bulk electronic conduction ($\sigma \sim 0.003$ S/cm at 400°C) by ~ one order of magnitude for $La_{1.5}Sr_{0.5}Ga_3O_{7.25}$. The oxygen loss in the melilite structure was verified and most likely takes place on the active interstitial oxide ions. The identified confinement space for electronic anions in melilite interstitial oxide ion conductors presented here provides a strategy to access inorganic electrides from interstitial oxide ion conductor electrolytes.

Keywords: Electride, Nonstoichiometric Melilite, Interstitial oxide ions, Topotactic reduction.

Introduction

Electrides that trap anionic electrons are an important class of ionic compounds demonstrating interesting chemical and physical properties such as strong reduction, metallicity, superconductivity, and catalytic activity owing to their unique electronic structures showing various anionic electron interconnectivity dimensionality from zero to three.[1, 2] Electrides are classified as inorganic and organic types depending on the constituting elements of the framework structures. Most of electrides suffer from poor stability at room temperature and in air, therefore the synthesis of stable electrides is still challenging. Owing to stability advantages over organic electrides, the synthesis of inorganic electrides and the exploration of their potential applications have received considerable attentions.[3] So far only a few inorganic electrides have been successfully prepared although theoretical studies predicted many more potential inorganic electrides.[4-6] The well-known examples of inorganic electrides includes calcium aluminate mayenite $Ca_{12}Al_{14}O_{33}$-based electrides (abbreviated as C12A7:e^-) ENREF 6 and dicalcium nitride Ca_2N compound ENREF 7 with various confinement spacings for anionic electrons covering from isolated to layered dimensionalities.[7, 8]

Among the known inorganic electrides, C12A7:e^- electrides have been standing at frontier of inorganic electrides owing to their outstanding thermal and chemical stability at room temperature in air and intriguing functions for various applications.[1] ENREF 1[9-13] $Ca_{12}Al_{14}O_{33}$ adopts a 3-dimensional (3D) tetrahedral network structure with subnanometer-sized cages which are partially occupied by extra oxygen atoms. The encaged oxygen atoms can be replaced by electron anions through topotactic reduction, leading to C12A7:e^- electrides with variable concentration of anionic electrons and therefore displaying different colors.[7] These electron anions are confined within the isolated cages, thus C12A7:e^- represents a zero dimensional (0D) electride which may work as electron field emitter and cathode materials for organic light emitting diodes.[11, 12] Initially, the anionic electrons in

C12A7:e^- was found to form diamagnetism[7] and later to display superconductivity with very low critical temperature 0.16-0.4 K, being the first example of electride superconductor.[13] The electron anions in C12A7:e^- can be replaced by hydride anions and the reversible storage and release of hydrogen in the cage make C12A7:e^- an efficient catalyst for ammonia synthesis at low temperature and ambient pressure when combined with the conventional Ru catalyst.[9, 14] However the recent investigation by Weber et al. concluded that the industrial application potential of C12A7:e^- as catalyst for the ammonia synthesis is limited due to the irreversible hydride formation at pressures > 1 MPa.[15] ENREF 7

As the topology of the confining cavity for anionic electrons has significant impact to the physical properties of electrides, it is important to identify new confinement spaces with unique topologies for anionic electrons in order to discover electrides with advanced performances.[8] The discovery of the C12A7:e^- electride by Hosono et. al.[7] provides a useful structural route to access new inorganic electrides from the known structure prototypes of oxides containing extra oxygen atoms, which are not bonded to the polyhedral framework, as well as the hardly reducible cations e.g. alkaline (earth) and aluminum cations through topotactic reduction. This strategy indeed applies to the recently theoretical-predicted $La_8Sr_2(SiO_4)_6$:$4e^-$ silicate apatite 1-dimensional (1D) electride,[16] which was synthesized partially through removing the 1D oxygen channels bonding with the La/Sr cations only. In the $Ca_{12}Al_{14}O_{33}$ mayenite structure, the encaged extra oxygen atoms display mobility at high temperatures leading to oxide ion conductivity properties comparable to those of yttrium-stabilized zirconia YSZ.[17] ENREF 15 The possibility to remove the mobile encaged oxygen atoms in the mayenite structure using topotactic reduction inspired our interest in interstitial oxide ion conducting electrolytes for discovery of new anionic electron confinement spacing and therefore oxide-based inorganic electrides. Indeed the environment for interstitial oxide ions could provide confinement

space for electrons if these interstitial oxide ions can be removed.

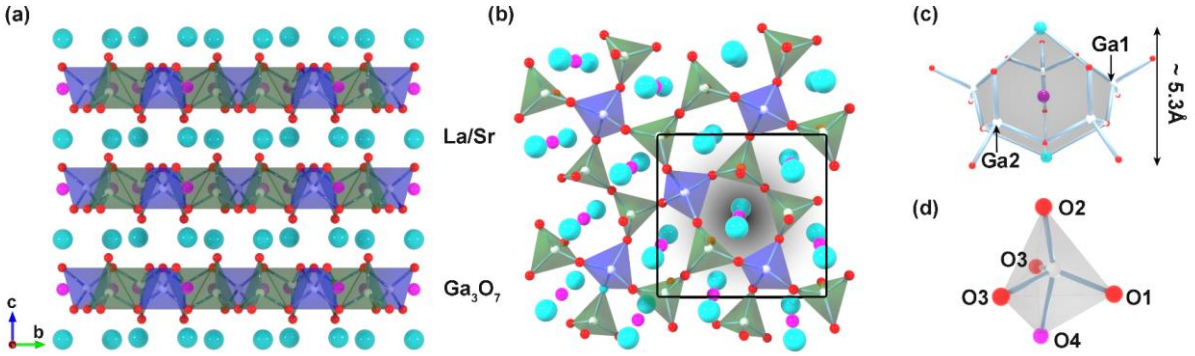

Figure 1. Crystal structure for interstitial oxide ion conducting gallate Melilite $LaSrGa_3O_7$. (a) Stacking of the (La/Sr) and (Ga_3O_7) layers along the *c* axis. (b) 2D $(Ga_3O_7)^{5-}$ corner-shared tetrahedral layer. (c) Cage confining the interstitial oxide ion (O4, pink) located in the five-fold rings and between two A cations. (d) Trigonal bipyramidal GaO_5 unit arising from incorporation of interstitial oxide ion.

The $LaSrGa_3O_7$ Melilite structure is composed of alternative large cationic (La/Sr) layers and corner-sharing Ga_3O_7 tetrahedral layers (Figure 1a), featuring five-fold tunnels consisting of five corner-sharing GaO_4 tetrahedra. The large (La/Sr) cations are eight-coordinated and located in the five-fold tunnels (Figure 1b).The gallate melilites have shown the ability to accommodate interstitial oxide ion defects with high mobility, which are incorporated into the non-planar five-fold rings and between two A cations (Figure 1c), transforming one of the tetrahedral GaO_4 with terminal oxygen (O2) in the ring into a trigonal bipyramidal GaO_5 (Figure 1d).[18] Recently, density function theory (DFT) calculations on the $La_{1.5}Sr_{0.5}Ga_3O_{7.25}$ composition revealed that the interstitial oxide ions have cooperatively weak antibonding interaction with framework oxygen atoms[19], which make interstitials oxide ions highly active, i.e. they are loosely bound with the framework, which could be favorable for chemical reduction. Herein we demonstrate in principle that interstitial oxide ions in the

pentagonal rings of the gallate melilites may be removed and replaced by electron anions which can be confined within the pentagonal rings and convert the melilite interstitial oxide ion conductors into 0D electrides and report its experimental verification. This work unravels a new cage-shaped confining space (Figure 1c) consisting of pentagonal rings and two A cations for the electron anions.

Methods

Synthesis. The $La_{1+x}Sr_{1-x}Ga_3O_{7+0.5x}$ (x = 0, 0.5) polycrystalline samples prior to the topotactic reduction were prepared by high−temperature solid−state reaction using La_2O_3 (99.99%, Aladdin), Ga_2O_3 (99.9%, Aladdin), and $SrCO_3$ (99.9%, Aladdin) as starting materials, which were weighed according to the correct stoichiometries with excess Ga_2O_3 (~ 3 mol%) and mixed thoroughly in ethanol using an agate mortar and pestle. The mixtures were preheated at 1200 ℃ for 12 h in air, then ground, uniaxially pressed into pellets and finally fired at 1400 ℃ for 12 h, leading to dense pellets with ~ 92% of X-ray theoretical densities.

The topotactic reduction of the $La_{1+x}Sr_{1-x}Ga_3O_{7+0.5x}$ (x = 0, 0.5) samples was performed using CaH_2 (Aladdin, > 98.5%) as a solid-state reducing agent. The as-made thin dense bulk ceramic samples (~ 1.4 mm thickness) from the high temperature sintering in air described above were buried in CaH_2 powder (according to the mass ratio of melilite to CaH_2, 0.5:1) in an argon-filled glovebox (O_2 and H_2O < 1 ppm), which were sealed in evacuated silica tubes and heated at various temperatures within 300–580 ℃ for 3–7 days for selecting the optimal temperature range for the topotactic reduction. The resulted pellets were washed with methanol solution of NH_4Cl (0.1 M) to remove the calcium-containing phases from ceramic surface (e.g., CaO and CaH_2) and dried under vacuum at room temperature. The high densities were retained for the reduced ceramic pellets, which were polished

to ensure further removal of surface impurities, and finally were used in the characterizations including the AC impedance spectroscopy measurements

Characterization. The phase formation in the samples was investigated by X-ray powder diffraction (XRD), which was performed on a Panalytical X'Pert Pro diffractometer (Cu Kα radiation) equipped with an Anton Paar oven chamber (HTK1600N). High-quality XRD data suitable for Rietveld refinement was collected over the 2θ range of 10-120˚ at room temperature. Variable temperature X-ray powder diffraction (VT-XRD) data were collected under air at room temperature and different temperatures with a 50 ℃ temperature step from 50 ℃ up to 1000 ℃ over the 2θ range from 10° to 80°. Neutron powder diffraction (NPD) data with a constant wavelength (λ = 1.225 Å) were collected at room temperature on the 3T2 powder diffractometer at the Laboratoire Léon Brilloin (Saclay, France) over a 2θ range of 5−120°. Rietveld refinements were performed on both XRD and NPD data using Topas Academic 6.0 [20] with the modified Thompson-Cox-Hastings pseudo-Voigt function for the profile refinement.[21, 22]

^{1}H solid-state nuclear magnetic resonance (NMR) experiments were performed on a Bruker Neo spectrometer operating at a magnetic field of 20.0 T corresponding to a ^{1}H Lamor frequency of 850 MHz. ^{1}H quantitative magic angle spinning (MAS) spectra were recorded at a spinning frequency of 30 kHz using a Hahn echo sequence. The echo delay was set to one rotor period (33.33 μs) and 32 transients were collected using a recycle delay of 3 s. The ^{1}H NMR spectra of the materials were obtained after subtracting the proton signal of an empty rotor recorded under the same experimental conditions.

The oxidation thermogravimetric analysis (TGA) was performed under atmosphere of O_2 at a flowing rate of 20 ml/min using a STA8000 thermal analyzer from 30 ℃ to 1000 ℃ to determine the

oxygen content in the topotactic reduced samples. Magnetization measurements were performed on a Quantum Design MPMS magnetometer under a 1000 Oe field while the samples were warmed from 2 K to 300 K, following zero−field cooling (ZFC) and field cooling (FC). AC Impedance spectroscopy (IS) measurements were carried out with a Solartron 1260A frequency response analyzer over the 10^{-1}–10^{6} Hz frequency range on the pellet samples placed between two silver electrodes on heating from 25 ℃ to 400 ℃ in a 5% H_2-95% N_2 atmosphere. X-ray photoelectron spectroscopy (XPS) measurements were carried out on an ESCALAB 250Xi spectrometer using Al Ka X-ray as the excitation source.

The optical diffuse reflectance data were collected in the 200-800 nm range using a Shimadzu (Kyoto, Japan) UV-3600 spectrometer equipped with an integrating sphere. Water reduction activity was examined under ultraviolet-visible (UV-Vis) light irradiation with a Xe lamp (350 W) or under dark in closed Pyrex cells. Typically, 0.5 g sample and 100 mL of the formic acid (0.1 M) containing chloroplatinic acid (2 *wt*% Pt) were added into the cell. Before irradiation, the mixture was treated with ultrasound for 10 min, and then aerated with N_2 bubbling for 25 min. The amount product H_2 was determined on a GC 1690-type gas chromatograph using N_2 gas as carrier for H_2 detection.

DFT calculations. The formation energies and electronic structures of interstitial-containing $La_{1.5}Sr_{0.5}Ga_3O_{7.25}$, as well as the reduced compositions $La_{1.5}Sr_{0.5}Ga_3O_7$ and $La_{1.5}Sr_{0.5}Ga_3O_{7.125}$ were investigated by density functional theory using Vienna Ab Initio Simulation Package (VASP, version 5.4.1).[23] Generalized gradient approximation (GGA) with Perdew-Burke-Ernzerhof functional (PBE)[24] and projector augmented wave (PAW) method were adopted for all the simulations. The plane-wave cutoff energy was set to 500 eV and a Γ-point of 4×4×3 was used for geometry optimization and 6×6×5 for electronic structure analysis to sample the first Brillouin zone. Geometry optimizations without structural constraints were carried out with convergence criterions for energy

and force at 1.0×10^{-5} eV/atom and 0.02 eV/Å, respectively. A 1×1×2 supercell (see models in Figure 2, a = 8.05 Å, c = 10.66 Å) with 49 atoms for $La_6Sr_2Ga_{12}O_{29}$ with interstitial oxide defects or 48 atoms for $La_6Sr_2Ga_{12}O_{28}$ without interstitial oxide defects and a 2×1×2 supercell was created by doubling the unit cell along the a-axis direction to realize the partial removal of interstitial oxide in composition $La_{12}Sr_4Ga_{24}O_{57}$ ($La_{1.5}Sr_{0.5}Ga_3O_{7.125}$). The valence states of the structures include $5s^25p^65d^16s^2$ for La atoms, $4s^24p^65s^2$ for Sr atoms, $3d^{10}4s^24p^1$ for Ga atoms and $2s^22p^4$ for O atoms. The interstitial oxide ion defect formation energies can be defined according to equation (1) and (2):[25]

$$La_4Sr_4Ga_{12}O_{28}(s) + La_2O_3(s) \rightarrow La_6Sr_2Ga_{12}O_{29}(s) + 2SrO(s) \quad (1)$$

$$\triangle H_f = [E(La_6Sr_2Ga_{12}O_{29}(s) + 2E(SrO(s))] - [E(La_4Sr_4Ga_{12}O_{28}(s)) + E(La_2O_3(s))] \quad (2)$$

Where E(X) is the total energy of the corresponding species.

The typically theoretical analyses for electrides including the density of states, band structures, 3D charge distribution and 2D electron localization function were performed with DFT calculations for the melilite compositions.[26-30] More details on the DFT calculations are provided in the supporting information.

Results and discussion

First, DFT calculations were performed on the $La_{1.5}Sr_{0.5}Ga_3O_7$ composition (here the interstitial oxide ions are completely removed) with $La_{1.5}Sr_{0.5}Ga_3O_{7.25}$ for comparison. Initially, the favorable structures for DFT calculations were searched based on the interstitials-containing $La_{1.5}Sr_{0.5}Ga_3O_{7.25}$ composition, and transferred to the reduced compositions. When La atoms replace Sr atoms to generate interstitial oxide ions for neutralization, the interstitial oxide ions may appear in the pentagonal ring between two La, two Sr or one La and one Sr. Based on these considerations, we constructed 6 possibly representative configurations in 1 × 1 × 2 supercells which contain one

interstitial oxygen for each supercell, as shown in Figure 2, and calculated their formation energies (ΔH_f) according to Eq. (2) through the geometry optimization. The calculations indicate that configurations 1 and 5 hold smaller formation energies compared with the other 4 configurations and configuration 5 has the lowest formation energy (Figure 2). Both configurations 1 and 5 were simulated in this study. However we present the results for configuration 1 in the main text taking the following three aspects into consideration: (i) La^{3+} shows higher positive charge than that of Sr^{2+}, which results in stronger electrostatic interactions with interstitial oxide ; (ii) besides, La^{3+} (r = 1.16 Å) holds smaller ionic radius compared with Sr^{2+} (r = 1.26 Å), indicating the smaller steric hindrance for the incorporation of interstitial oxide ions[31] (iii) there are more La-O_i-La configurations than La-O_i-Sr or Sr-O_i-Sr configurations in $La_{1.5}Sr_{0.5}Ga_3O_{7.25}$ from a statistical point of view. The theoretical simulation results of configurations 5 are provided in the supporting information (Figure S1 and S2).

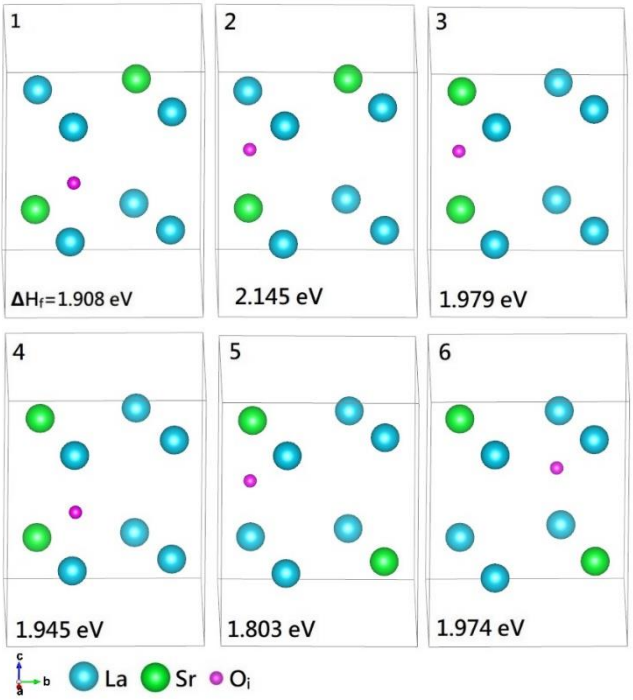

Figure 2. The 6 configurations in 1 × 1 × 2 supercells illustrating different distributions of La, Sr and interstitial oxide ion (O_i) in $La_{1.5}Sr_{0.5}Ga_3O_{7.25}$ composition and their corresponding formation energies ΔH_f calculated according to equations (1) and (2). O and Ga atoms are not displayed for

clarity.

Figure 3 shows the band structures, total density of states (TDOS) and partial/projected density of states (PDOS) of $La_{1.5}Sr_{0.5}Ga_3O_{7.25}$ and $La_{1.5}Sr_{0.5}Ga_3O_7$. In $La_{1.5}Sr_{0.5}Ga_3O_{7.25}$, the valance band maximum (VBM) is mainly composed of O/O_i 2*p* orbitals and 4*s/p/d* orbitals of Ga atoms in the surrounding pentagonal rings, while the conduction band minimum (CBM) mainly consists of La 4*f* orbitals, as shown in Figure 3b. The overlaps between Ga 3*d* and O 2*p* orbitals indicate the covalent Ga-O bonds in polyhedral network. After the removal of O_i atoms, a new occupied band emerges in the forbidden band of $La_{1.5}Sr_{0.5}Ga_3O_{7.25}$, presumably associated with the anionic electrons. In order to visualize the contribution of anionic electrons, we placed a pseudoatom with a Wigner-Seitz radius of 1.509 Å (labeled as X) in $La_{1.5}Sr_{0.5}Ga_3O_7$ at the sites previously occupied by the interstitial oxide ion defects. This strategy is typical one employed for the theoretical investigation of elecrides.[27, 28, 30, 32] The contribution of interstitial oxide ion O_i in $La_{1.5}Sr_{0.5}Ga_3O_{7.25}$ and anionic electron X in $La_{1.5}Sr_{0.5}Ga_3O_7$ are highlighted in pink in Figure 3 a, c and the first two panels of Figure 3 b, d. From Figure 3a we can see that the interstitial oxide ion O_i in $La_{1.5}Sr_{0.5}Ga_3O_{7.25}$ occupies two channel bands just below the Fermi level and the band gap is 2.87 eV, while a new channel band emerges in the forbidden band associating with anionic electron X in $La_{1.5}Sr_{0.5}Ga_3O_7$ (Figure 3c) and thus the bandgap is narrowed to 0.63 eV. In Figure 3d one can clearly see that an interstitial band fluctuating 1 eV below the Fermi level appears and associates with interstitial electron X after the removal of O_i atoms, which confirms the presence of anionic electron in $La_{1.5}Sr_{0.5}Ga_3O_{7.25}$. Accordingly, the Fermi energy level shifts from 3.84 eV in $La_{1.5}Sr_{0.5}Ga_3O_{7.25}$ to 6.46 eV in $La_{1.5}Sr_{0.5}Ga_3O_7$ as a result of the emerging bands associated with anionic electrons. The location of extra electrons was analyzed by the electron localization function calculation below. More TDOS comparison between $La_{1.5}Sr_{0.5}Ga_3O_{7.25}$ and $La_{1.5}Sr_{0.5}Ga_3O_7$ are provided in Figure S3.

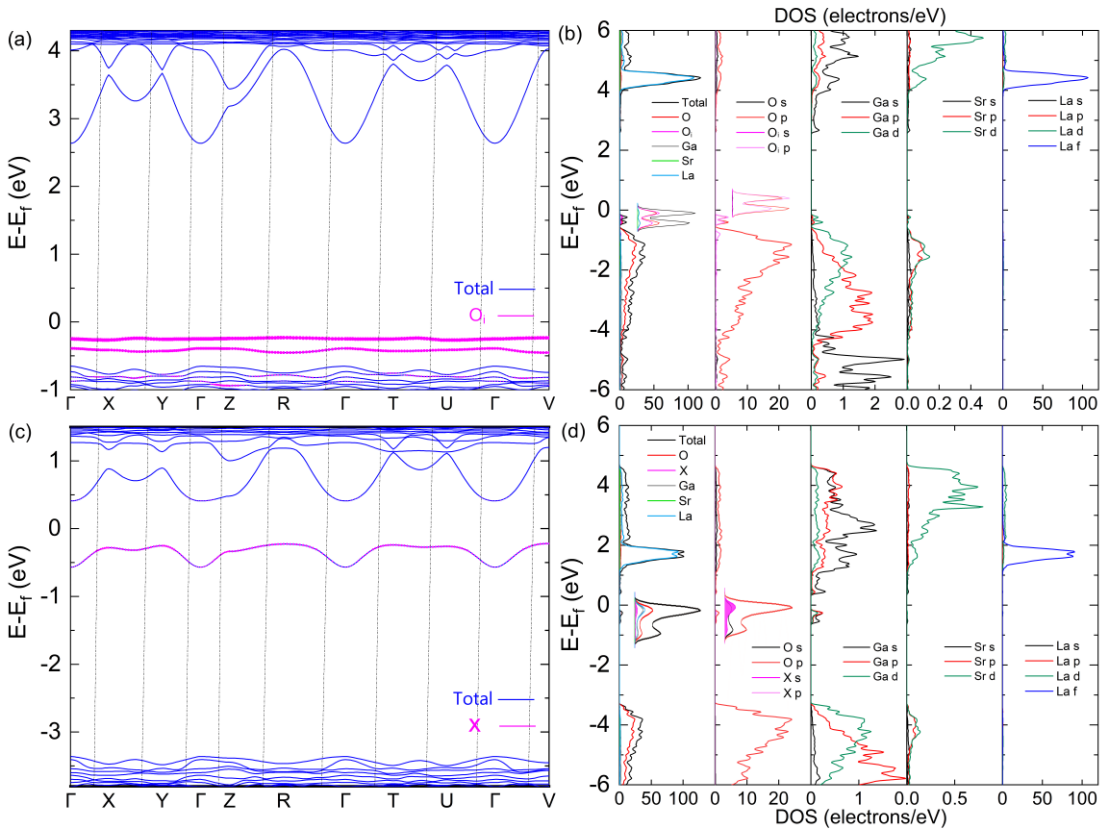

Figure 3. (a, c) Band structures and (b, d) total density of states (TDOS) and partial/projected density of states (PDOS) of (a, b) $La_{1.5}Sr_{0.5}Ga_3O_{7.25}$ and (c, d) $La_{1.5}Sr_{0.5}Ga_3O_7$ with the contribution of interstitial oxide ion O_i and anionic electron X highlighted in pink. The TDOS/PDOS below 1 eV of the fermi level are enlarged in the first two panels of (b) and (d), highlighting the contribution of interstitial oxide ion O_i and anionic electrons X. The structures are based on configuration 1 in with a 1×1×2 supercell in Figure 2.

Electron localization function (ELF) calculated with DFT method can be a reliable theoretical descriptor for us to evaluate whether the electrons left by the escaped interstitial oxide ions are caged as anions in the reduced $La_{1.5}Sr_{0.5}Ga_3O_7$, i.e. $La_{1.5}Sr_{0.5}Ga_3O_7$ forms as electride.[29, 33] The values of ELF are at the range of 0 ~ 1: 0 indicates that the electrons are highly delocalized or there is no electron, while 1 indicates totally localized electrons. Figure 4 a and e show the optimized structures of $La_{1.5}Sr_{0.5}Ga_3O_{7.25}$ and $La_{1.5}Sr_{0.5}Ga_3O_7$, respectively. The three-dimensional (3D) plot of ELF distribution results reveals that in $La_{1.5}Sr_{0.5}Ga_3O_7$ the electrons are highly localized at the position of

interstitial oxygen after its removal (Figure 4 b, f), i.e., the electrons left by the escaped interstitial oxygen atoms are indeed caged, the integrated extra caged electron is about 0.88 e^-. In order to observe the caged electrons more easily, we plot two-dimensional (2D) maps of ELF distribution along (001) plane and the corresponding max ELF value is about 0.74, which shows that the interstitial electrons are located at the center of the pentagonal ring. Thus, the reduced $La_{1.5}Sr_{0.5}Ga_3O_7$ can be described as an electride and formulated as $4(La_{1.5}Sr_{0.5}Ga_3O_7):2e^-$.

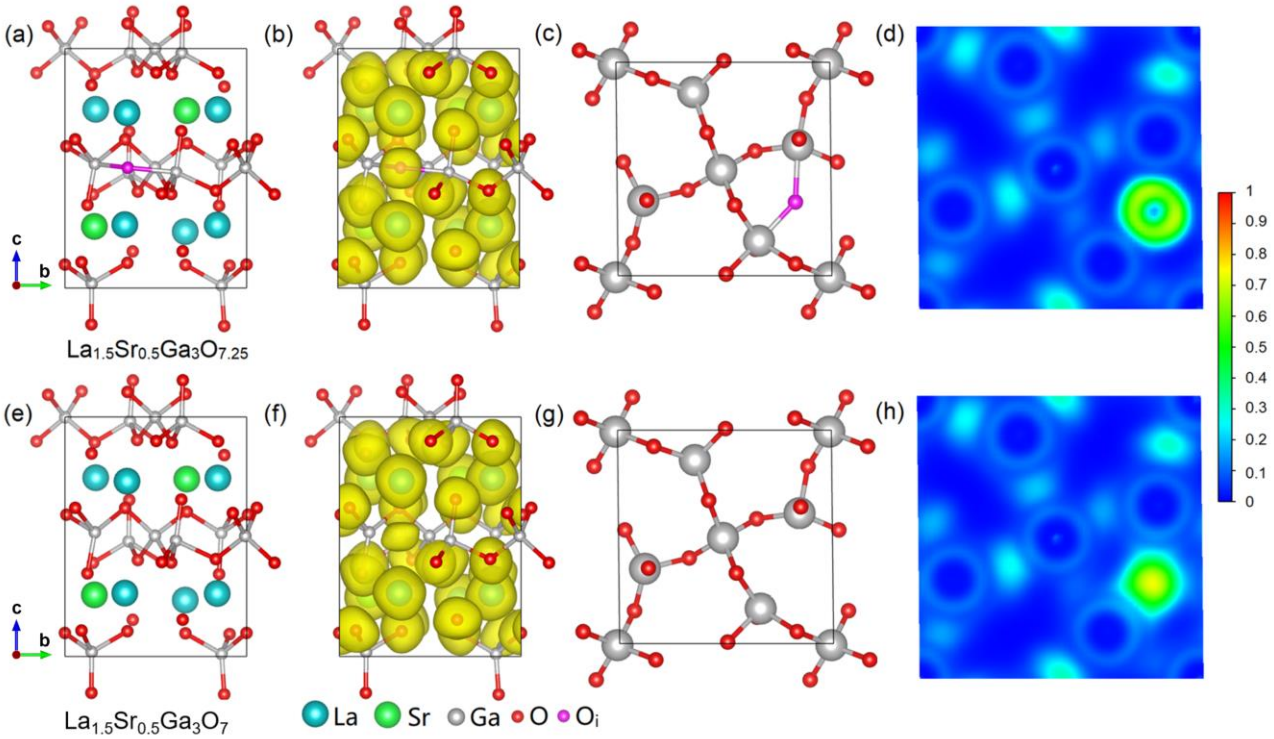

Figure 4. Optimized structures and computed ELF distributions of (a-d) $La_{1.5}Sr_{0.5}Ga_3O_{7.25}$ and (e-h) $La_{1.5}Sr_{0.5}Ga_3O_7$ based on configuration 1: (a, e) the optimized 1×1×2 supercell; (b, f) the 3D plot of ELF distribution, showing a 0.3 au isosurface; (c, g) unit-cell geometry at (001) plane; (d, h) the 2D plots map of ELF distribution along (001) plane.

In order to produce an electride material from $La_{1.5}Sr_{0.5}Ga_3O_{7.25}$, topotactic reduction was performed on $La_{1.5}Sr_{0.5}Ga_3O_{7.25}$ containing interstitial oxygen at various temperatures ranging from 300 ℃ to 580 ℃ using CaH_2 as reducing agent. The samples reduced at various temperatures display

similar XRD patterns with that for the as-made one (Figure 5a), except for partial decomposition due to over-reduction at 580 ℃, which resulted in a small amount of La_2O_3 and $LaSrGaO_4$ phases (Figure 5a and S4a). With the increase of the reduction temperature, the color of $La_{1.5}Sr_{0.5}Ga_3O_{7.25}$ sample gradually changed from white to black, as show Figure 5b. In contrast with the interstitials-containing composition, the reduction of the parent $LaSrGa_3O_7$ without interstitial oxygen at 580 ℃, did not much change the color (Figure 5c) and phase (Figure S5) of the sample. The ease to reduce the interstitials-containing nonstoichiometric composition compared with the stoichiometric composition may therefore be ascribed to the existence of interstitial oxide ions. In other words, the interstitials oxide ions are more active than the framework oxide ions in the melilite structure. The refined cell parameters of the samples before and after reduction are almost identical except for the slightly smaller cell volume for the $La_{1.5}Sr_{0.5}Ga_3O_{7.25-\delta}$ sample reduced at 580 ℃ (Figure S6), on which the following characterizations were performed if not specified.

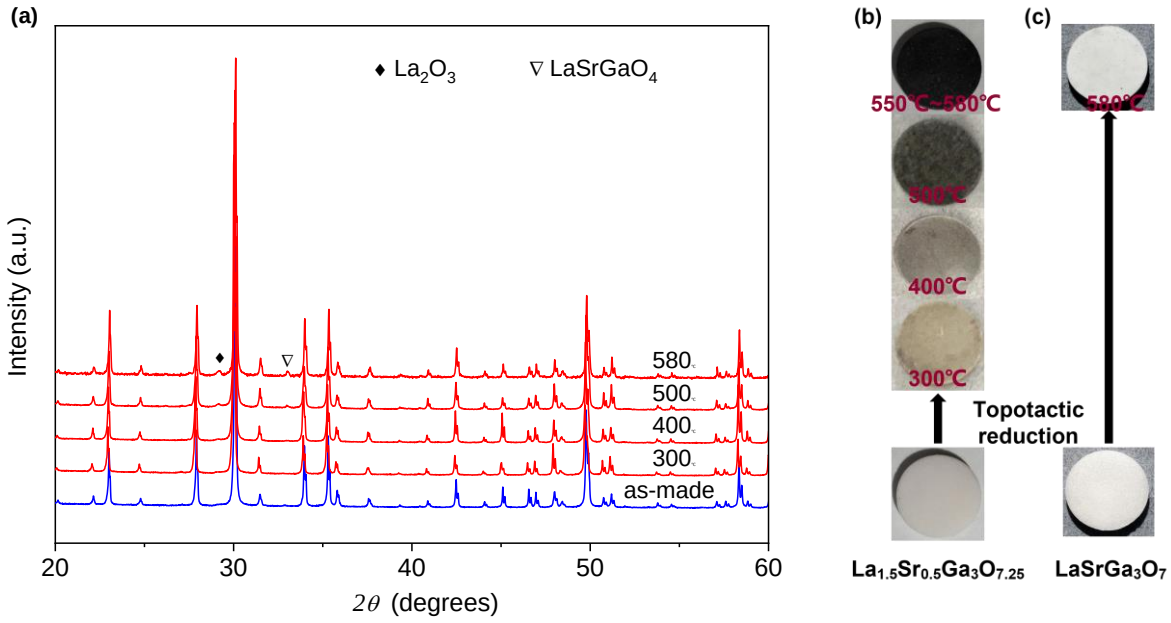

Figure 5. (a) XRD patterns and (b) color evolution of the $La_{1.5}Sr_{0.5}Ga_3O_{7.25-\delta}$ samples reduced at different temperatures in comparison with the as-made one. (c) Photographs of $LaSrGa_3O_7$ samples before and after reduction at 580 ℃.

In order to examine whether the H^- hydride anion was incorporated into the melilite structure and the Ga valence change in $La_{1.5}Sr_{0.5}Ga_3O_{7.25}$ during the CaH_2 reduction, ^1H MAS NMR and XPS measurements were carried out. As shown in Figure S7, ^1H MAS NMR measurements excluded the possibility of H^- hydride anion in the melilite structure.[34] The XPS data show apparent existence of metal Ga signal in the reduced $La_{1.5}Sr_{0.5}Ga_3O_{7.25-\delta}$ samples (Figure S8). The EDS element mapping for the reduced samples (Figure S9) show that there is aggregation of Ga at the surface of the ceramic sheet, confirming that the topotactic reduction partially reduces the melilite materials to produce metal Ga. It should be noted here that the high Ga metal content from the XPS data does not means that most of Ga^{3+} in the samples was reduced to Ga metal as the XPS only probes the sample surface (only a thickness of a few nanometers). Moreover Ga metal is liquid at room temperature, therefore easily immersing the grains along the surface. The total Ga content in the reduced samples is rather limited as indicated by the TGA data and water reduction characterization described below.

The existence of Ga metal in the reduced $La_{1.5}Sr_{0.5}Ga_3O_{7.25-\delta}$ samples was also confirmed by the magnetism measurement, which show normal diamagnetic behavior above 10 K but significantly enhanced diamagnetic susceptibilities below 7.22 K (Figure 6 a-b). This behavior could be ascribed to the superconductivity of metal Ga in the reduced samples. However, the reduced samples were found to be highly resistive all through the low temperature region below room temperature, which confirms that the reduced samples had very low contents of Ga metal, which did not connect with each other in the reduced samples to produce the short circuit effect. On the other hand, the as-made sample displayed single $2p_{3/2}$ and $2p_{1/2}$ XPS peaks for Ga 2*p* orbits (Figure S8b) and diamagnetic behavior as normal, followed by a transition to paramagnetic substance below 7.22 K (Figure 6c). Such magnetic behavior suggests absence of Ga metal in the as-made sample. Therefore, the XPS

peaks for Ga 2*p* orbits all come from Ga^{3+} instead of the mixed Ga and Ga^{3+} found in the reduced samples.

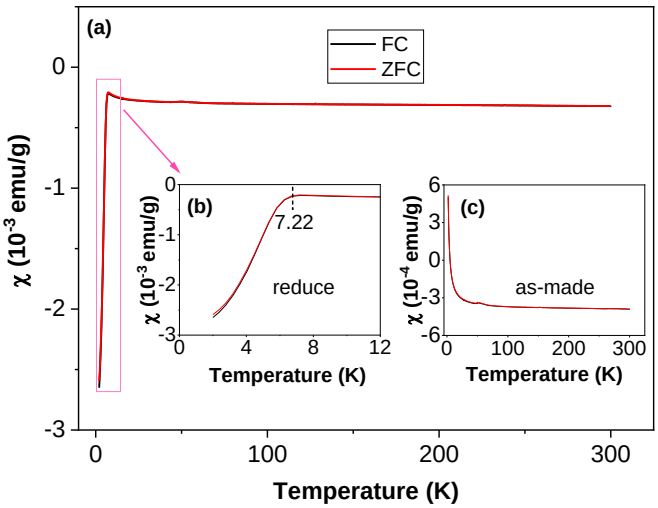

Figure 6. (a) χ vs temperature plot for the reduced $La_{1.5}Sr_{0.5}Ga_3O_{7.25-\delta}$ recorded in the ZFC and FC modes. The insets from left to right show an enlarged view of (b) the diamagnetic enhancement of the reduced $La_{1.5}Sr_{0.5}Ga_3O_{7.25-\delta}$ at 7.22 K and (c) χ~ T plot of the as-made $La_{1.5}Sr_{0.5}Ga_3O_{7.25}$, respectively.

Thermal gravimetric analysis (TGA) was performed on the reduced $La_{1.5}Sr_{0.5}Ga_3O_{7.25-\delta}$ samples in O_2, which showed a change in color from black to white and an associated weight increase ~ 0.51 *wt*% (Figure S10). This mass gain started from about 400 °C, is ascribed to reoxidation of the reduced $La_{1.5}Sr_{0.5}Ga_3O_{7.25-\delta}$ sample, from which the removed oxygen content δ per formula can be calculated as 0.18, assuming that the mass gain was completely from the reoxidation of reduced melilite phase. The reoxidation of the sample was also confirmed by the VT-XRD experiment in air (Figure S11), showing that the sample retained the tetragonal melilite structure after oxidation, except for the formation of $LaGaO_3$, probably due to the volatilization of Ga_2O_3 at high temperatures. Although there was no apparent Ga_2O_3 phase observed in the VT-XRD data during the oxidation procedure,

the oxidation of Ga metal to Ga_2O_3 can take place from ~ 400 °C and the Ga_2O_3 could appear as amorphous. Apart from this, there could be still oxygen uptake for the melilite phase, i.e., the oxygen atoms in the melilite phase could be removed partially during the topotactic reduction and the reoxidation occurred for the melilite phase as well. Considering that the stoichiometric $LaSrGa_3O_7$ is hard to be reduced, the interstitial oxide ions are suspected to be removed during the topotactic reduction of in $La_{1.5}Sr_{0.5}Ga_3O_{7.25}$. Although the Ga metal content and the removed oxygen content in the melilite phase (which is lower than the determined δ value per formula above) are not able to be discerned from the oxygen-oxidation TGA data, the electrons associated with the oxidation can be determined as 6.25×10^{-4} electrons per 1g reduced sample.

The reduced $La_{1.5}Sr_{0.5}Ga_3O_{7.25-\delta}$ samples were found to react with water under dark environments, producing hydrogen gas (Figure 7). The hydrogen evolution can be enhanced by both visible and UV light radiation. However no apparent hydrogen evolution was observed at the visible and UV light radiation time exceeding 8 hours. This result indicates that the reduced samples do not have real photocatalytic activity and the hydrogen evolution could be mainly arising from the reactivity of metallic gallium with the water. The enhanced hydrogen evolution under light irradiation may be ascribed to the light absorbance of the sample accelerating the electron releasing from the metallic Ga and therefore the reduction reaction. The electrons associated with the saturated hydrogen evolution under light radiation (Figure 7) was estimated as 3.67×10^{-4} electrons per 1g reduced sample. This value is smaller than that (6.25×10^{-4} electrons per 1g reduced sample) associated with the oxidation determined from the TGA data above. The discrepancy between the electron numbers from different experiments could not be unmeaningful and the possibility that some electrons in the reduced sample did not participate the hydrogen evolution can not be excluded completely, which could be in the melilite phase.

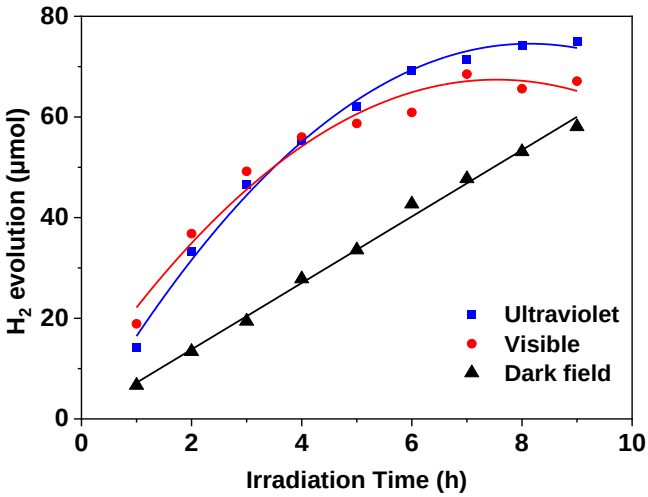

Figure 7. Hydrogen evolution over the reduced $La_{1.5}Sr_{0.5}Ga_3O_{7.25-\delta}$ sample in the formic acid solution under irradiation of UV and visible lights in comparison with the dark environment.

NPD data were collected on 6g reduced $La_{1.5}Sr_{0.5}Ga_3O_{7.25-\delta}$ sample, which was obtained through gathering the products from different reduction batches. Rietveld refinement of NPD data (Figure S12) was performed based on the average structural model of $La_{1.54}Sr_{0.46}Ga_3O_{7.27}$,[18] to analyze the oxygen content in the reduced product, which converged to $R_{wp} \approx 4.29\%$ and $R_p \approx 3.36\%$. The occupancies for the oxygen sites were freely refined, which showed that the framework oxygen sites are essentially fully occupied (The refined occupancies were 0.98(1), 1.00(8) and 0.996(8) for O1, O2 and O3, respectively and fixed as units) and the interstitial O4 site has an occupancy of 9.4(4)% (its refined atomic displacement factor B_{iso} is 0.5(3) $Å^2$, Table S1), apparently lower than that (12.5%) corresponding to the pristine $La_{1.5}Sr_{0.5}Ga_3O_{7.25}$ composition.[18] When the occupancy of O4 was fixed at 12.5% (corresponding to the full interstitial oxide ion content without reduction), its refined B_{iso} increased to 1.45 $Å^2$ with the reliability factors slightly increased to $R_{wp} \approx 4.36\%$ and $R_p \approx 3.42\%$. Considering that the occupancy is highly correlated with the atomic displacement factor, we cannot determine precisely the interstitial oxygen loss based on the structural analysis on NPD data. It should

be noted here that there are still some misfits in the NPD data fitting (Figure S12). Such misfit could be ascribed to the positional disorder of framework atoms arising from the incorporation of interstitial oxide ion, which is beyond description of the average structure model employed here.[18]

In order to examine how the reduction affects the electrical conductivities of $La_{1.5}Sr_{0.5}Ga_3O_{7.25}$, AC impedance data of the reduced $La_{1.5}Sr_{0.5}Ga_3O_{7.25-\delta}$ pellet were collected on the as-made $La_{1.5}Sr_{0.5}Ga_3O_{7.25}$ pellet for comparison. Figure 8a shows the typical complex impedance plot of the as-made $La_{1.5}Sr_{0.5}Ga_3O_{7.25}$ at 150 ℃, which consists of a semicircular arc from bulk response with capacitances ~ 10^{-12}-10^{-11} F/cm and a Warburg-type electrode response with large capacitances ~ 10^{-8}–10^{-7} F/cm in the low frequency range, consistent with the oxide ion conduction.[35] There is intermediate arc between the bulk and electrode response arcs, showing ~ 10^{-10} F/cm capacitances, indicative of grain boundary response. The bulk response arcs can be modeled with an equivalent circuit consisting of three parallel R_b, C_b, and $(CPE)_b$ elements (b is for bulk, and CPE is a constant phase element).[36] The fitted C_b is ~ 7 pF/cm , consistent with the bulk response. While for the reduced $La_{1.5}Sr_{0.5}Ga_3O_{7.25-\delta}$ sample, the high-frequency arc showed capacitances covering from 10^{-12} F/cm to 10^{-10} F/cm at 150 ℃ indicating overlapped bulk and grain boundary response arcs, which cannot be accurately distinguished even by equivalent circuit modeling, and a bended Warburg-type electrode response arc (Figure 8b), indicative of mixed electronic and ionic conduction.

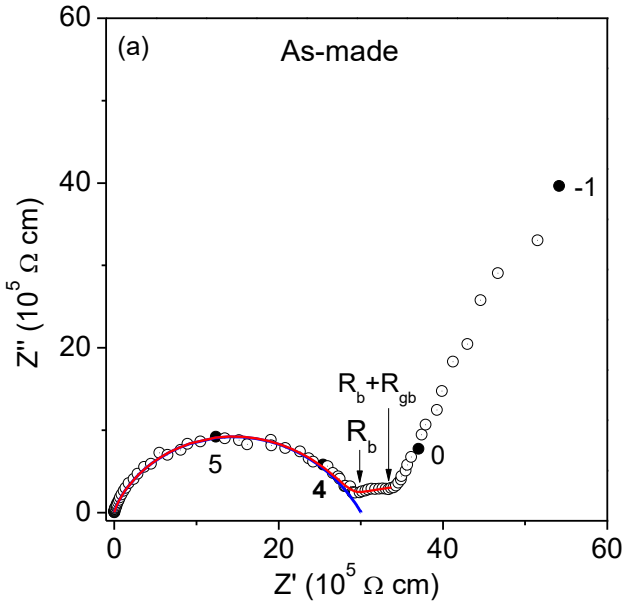
(a)
As-made
Z'' (10^5 Ω cm)
Z' (10^5 Ω cm)
R_b+R_{gb}
R_b
-1
0
4
5

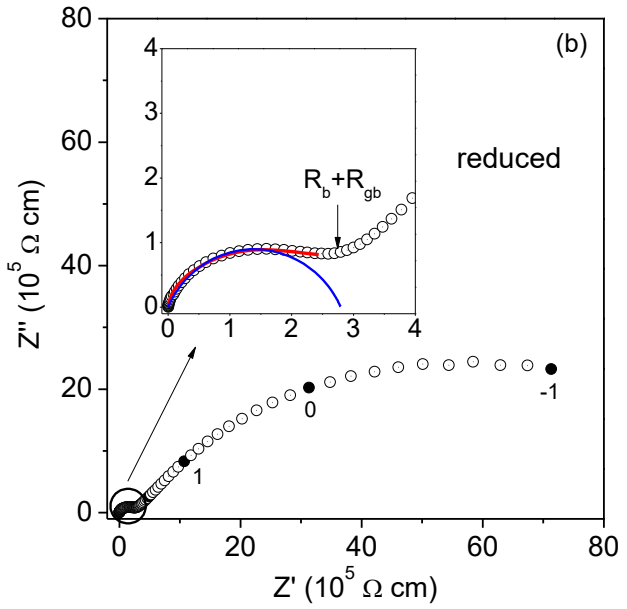
(b)
reduced
Z'' (10^5 Ω cm)
Z' (10^5 Ω cm)
R_b+R_{gb}
-1
0
1

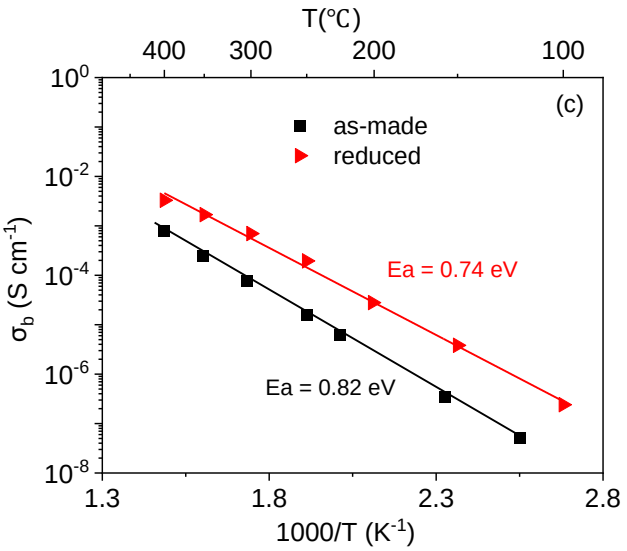
T(℃)
(c)
as-made
reduced
Ea = 0.74 eV
Ea = 0.82 eV
σ_b (S cm^{-1})
1000/T (K^{-1})

Figure 8. (a, b) The typical complex impedance plots at 150℃ and (c) bulk conductivities of (a) the as-made and (b) reduced $La_{1.5}Sr_{0.5}Ga_3O_{7.25-\delta}$ samples. The solid lines in red and blue in (a) and (b) are respectively fitted and simulated (for bulk response only in (a) and for mixed bulk and grain boundary responses in (b)) lines. The inset in (b) enlarges the high-frequency arc. R_b and R_{gb} denote the bulk and grain boundary resistivities, respectively. The numbers denote logarithms of the selected frequencies.

Figure 8c shows the total conductivities of the reduced $La_{1.5}Sr_{0.5}Ga_3O_{7.25-\delta}$ sample, varying within 10^{-7}-10^{-3} S/cm from 100 ℃ to 400 ℃, which is ~ 1 order of magnitude higher than the bulk conductivities for the as-made $La_{1.5}Sr_{0.5}Ga_3O_{7.25}$. This result reveals that the bulk conductivities of reduced sample are higher than that for the as-made sample. Accordingly, the reduced sample displayed lower activation energy (E_a) ~ 0.74 eV than that (~ 0.82 eV) for the as-made materials. Here the influence of phase decomposition on the electrical conduction behavior upon the reduction is considered to be limited based on the following three aspects. (i) The electrically insulating nature of the reduced samples above room temperature confirms the low content of Ga metal and the Ga metal liquid appeared isolated. Therefore, the metallic gallium certainly is not the case causing the enhanced bulk conductivity. (ii) Given the low contents (covering from ~ 0.7% to ~ 4% from NPD and XRD data) for $LaSrGaO_4$ and La_2O_3 phases in the reduced samples and their much lower conductivity than the melilite oxide ion conductors, it is unlikely that the enhanced conductivity arose from these two phases.[37, 38] ENREF 38 ENREF 38 ENREF 38 (iii) The existence of lanthanum hydroxide was considered here as this phase was observed in the powder sample for the NPD experiment. However, the pellets for the impedance measurement of the reduced sample were obtained through burying the as-made dense pellets in CaH_2 powder. The dense nature of the pellets was retained after the reduction. The moisture in air is hardly to go through such dense pellets during the impedance

measurement at high temperature. No apparent lanthanum hydroxide phase was observed in the XRD data of the pellet collected before and after the impedance measurement. Thus, neither the lanthanum hydroxide phase contributed to the enhanced conductivity. In short words, it is highly likely that the enhanced bulk conductivity upon reduction is due to the topotactic reduction of the melilite phase, rather than the decomposition. In other words, the oxygen loss in the melilite phase could indeed took place topotactically in the reduction of $La_{1.5}Sr_{0.5}Ga_3O_{7.25}$ although it is mild. Taking the mixed conduction observed from the impedance data into consideration, the enhanced bulk conductivity for the reduced sample comes from the contribution of electronic conductivity, which could arise from the electrons left by the escaped oxide ions in the melilite phase upon reduction. As indicated by the hardly reducible nature for the parent $LaSrGa_3O_7$ and the structural analysis on the NPD data described above, oxygen loss is highly likely on the active interstitial oxide ions rather than the framework oxide ions, given that the loss of framework oxide ions will break the corner-sharing connectivity for the tetrahedral layer, and the removing of interstitial oxygen atoms in $La_{1.5}Sr_{0.5}Ga_3O_{7.25}$ does not change the framework at all.

ENREF 33 Considering that the interstitial oxides were not completely reduced during topotactic reduction, we have also constructed a 2×1×2 supercells to simulate $La_{1.5}Sr_{0.5}Ga_3O_{7.125}$ using configuration 1 to probe the electronic structure in the partially reduced melilite. This composition shared similar results on the electronic structure (Figure S13) and ELF value (Figure S14) with those of 1×1×2 supercell for $La_{1.5}Sr_{0.5}Ga_3O_7$. This means that when the individual interstitial oxide ion is removed, the electrons left by the escaped oxygen still act as anionic electrons, leading to nonstoichiometric electride.

Conclusion

DFT ELF calculations indicated that the interstitial oxide ions in the pentagonal rings of the gallate melilites may be removed and replaced by electron anions, which are confined within the pentagonal rings and convert the melilite interstitial oxide ion conductor into 0D electrides. In contrast with the hardly reducible nature for the parent $LaSrGa_3O_7$, the topotactic reduction of $La_{1.5}Sr_{0.5}Ga_3O_{7.25}$ by CaH_2 resulted in black product with small amount of Ga^{3+} reduced to Ga metal. This reveals that interstitials oxide ions are more active than the framework oxide ions, making the melilite structure more reducible. The enhanced bulk electronic conduction by ~ one order of magnitude in the reduced samples verified the oxygen loss in the melilite structure during the topotactic reduction, which was highly likely on the active interstitial oxide ions. The new confinement space for electronic anions identified from the melilite interstitial oxide ion conductors in this work suggests that more interstitial oxide ion conductor electrolytes can be candidate hosts for preparation of new inorganic electrides.

ASSOCIATED CONTENT

Supporting information

Comparison on DOS, optimized structures and computed ELF distributions of $La_{1.5}Sr_{0.5}Ga_3O_{7.25}$ and $La_{1.5}Sr_{0.5}Ga_3O_7$ based on configuration 5; Comparison of the TDOS between $La_{1.5}Sr_{0.5}Ga_3O_{7.25}$ and $La_{1.5}Sr_{0.5}Ga_3O_7$/$La_{1.5}Sr_{0.5}Ga_3O_{7.125}$ based on configurations 1 and 5; Comparison on DOS, optimized structures and computed ELF distributions of $La_{1.5}Sr_{0.5}Ga_3O_{7.25}$ and $La_{1.5}Sr_{0.5}Ga_3O_{7.125}$ based on configuration 1; XRD patterns and Ga 2p XPS spectra of the as-made and reduced $LaSrGa_3O_7$ samples; Rietveld plots for XRD data and the cell parameters of the reduced $La_{1.5}Sr_{0.5}Ga_3O_{7.25-\delta}$ and

$LaSrGa_3O_7$ products; in−situ variable temperature XRD patterns, ^1H MAS NMR spectra, Rietveld plot for NPD data, the final refined structural parameters, EDS elemental mapping and thermogravimetric data in oxygen atmosphere of the reduced $La_{1.5}Sr_{0.5}Ga_3O_{7.25-\delta}$. This information is available free of charge at https://pubs.acs.org/.

Author Contributions

Lijia Zhou and Jinxiao Zhang contributed equally.

Notes

The authors declare no competing financial interest.

Acknowledgement

National Natural Science Foundation of China (No. 22090043, 21622101, 22103019), Guangxi Natural Science Foundation (No. 2019GXNSFGA245006), Guangxi Key Laboratory of Electrochemical and Magneto-chemical Functional Materials (No. EMFM20211111) are acknowledged for the financial support. The authors thank Florence PORCHER for neutron experiments realized at the Laboratoire Léon Brillouin in Saclay, France and Prof. Xing Ming for the valuable discussion on the DFT calculation results.

References

1. Zhang, X.; Yang, G. Recent Advances and Applications of Inorganic Electrides. *J. Phys. Chem. Lett.* **2020,** 11, 3841-3852.

2. Liu, C.; Nikolaev, S. A.; Ren, W.; Burton, L. A. Electrides: a review. *J. Mater. Chem. C* **2020,** 8, 10551-10567.

3. Dye, J. L. Electrons as Anions. *Science* **2003,** 301, 607-608.

4. Srdanov, V. I.; Haug, K.; Metiu, H.; Stucky, G. D. (Na_4^{3+}) clusters in sodium sodalite. *J. Phys. Chem.* **1992,** 96, 9039-9043.

5. Ichimura, A. S.; Dye, J. L.; Camblor, M. A.; Villaescusa, L. A. Toward inorganic electrides. *J. Phys. Chem. Lett.* **2002,** 124, 1170-1171.

6. Wernette, D. P.; Ichimura, A. S.; Urbin, S. A.; Dye, J. L. Inorganic electrides formed by alkali metal addition to pure silica zeolites. *Chem. Mater.* **2003,** 15, 1441-1448.

7. Matsuishi, S.; Toda, Y.; Miyakawa, M.; Hayashi, K.; Kamiya, T.; Hirano, M.; Tanaka, I.; Hosono, H. High-density electron anions in a nanoporous single crystal: $[Ca_{24}Al_{28}O_{64}]^{4+}(4e^-)$. *Science* **2003,** 301, 626-629.

8. Lee, K.; Toda, Y.; Matsuishi, S.; Hosono, H.; Kim, S. W. Dicalcium nitride as a two-dimensional electride with an anionic electron layer. *Nature* **2013,** 494, 336-340.

9. Kitano, M.; Inoue, Y.; Yamazaki, Y.; Hayashi, F.; Kanbara, S.; Matsuishi, S.; Yokoyama, T.; Kim, S. W.; Hara, M.; Hosono, H. Ammonia synthesis using a stable electride as an electron donor and reversible hydrogen store. *Nat. Chem.* **2012,** 4, 934-940.

10. Toda, Y.; Hirayama, H.; Kuganathan, N.; Torrisi, A.; Sushko, P. V.; Hosono, H. Activation and splitting of carbon dioxide on the surface of an inorganic electride material. *Nat. Commun.* **2013,** 4, 2378.

11. Toda, Y.; Kim, S. W.; Hayashi, K.; Hirano, M.; Kamiya, T.; Hosono, H.; Haraguchi, T.; Yasuda, H. Intense thermal field electron emission from room-temperature stable electride. *Appl. Phys. Lett.* **2005,** 87, 254103.

12. Kim, K.-B.; Kikuchi, M.; Miyakawa, M.; Yanagi, H.; Kamiya, T.; Hirano, M.; Hosono, H. Photoelectron Spectroscopic Study of C12A7:e^- and Alq_3 Interface: The Formation of a Low Electron-Injection Barrier. *J. Phys. Chem. C* **2007,** 111, 8403-8406.

13. Miyakawa, M.; Kim, S. W.; Hirano, M.; Kohama, Y.; Kawaji, H.; Atake, T.; Ikegami, H.; Kono, K.; Hosono, H. Superconductivity In An Inorganic Electride $12CaO{\cdot}7Al_2O_3{:}e^-$. *J. Am. Chem. Soc.* **2007,** 129, 7270-7271.

14. Hayashi, K.; Matsuishi, S.; Kamiya, T.; Hirano, M.; Hosono, H. Light-induced conversion of an insulating refractory oxide into a persistent electronic conductor. *Nature* **2002,** 419, 462-465.

15. Weber, S.; Schäfer, S.; Saccoccio, M.; Ortner, N.; Bertmer, M.; Seidel, K.; Berendts, S.; Lerch, M.; Gläser, R.; Kohlmann, H. Mayenite-Based Electride C12A7e−: A Reactivity and Stability Study. *Catalysts* **2021,** 11, 334.

16. Zhang, Y.; Xiao, Z.; Kamiya, T.; Hosono, H. Electron Confinement in Channel Spaces for One-Dimensional Electride. *J. Phys. Chem. Lett.* **2015,** 6, 4966–4971.

17. Lacerda, M.; Irvine, J. T. S.; Glasser, F. P.; West, A. R. High oxide ion conductivity in $Ca_{12}Al_{14}O_{33}$. *Nature* **1988,** 332, 525-526.

18. Kuang, X.; Green, M. A.; Niu, H.; Zajdel, P.; Dickinson, C.; Claridge, J. B.; Jantsky, L.; Rosseinsky, M. J. Interstitial oxide ion conductivity in the layered tetrahedral network melilite structure. *Nat. Mater.* **2008,** 7, 498-504.

19. Xu, J. G.; Li, Y. C.; Zhou, L. J.; Tang, X.; Kuang, X. J. Chemical Bonding Effect on the Incorporation and Conduction of Interstitial Oxide Ions in Gallate Melilites. *Adv. Theor. Simul.* **2019,**

2, 1900069.

20. Coelho, A. A. TOPAS and TOPAS-Academic: an optimization program integrating computer algebra and crystallographic objects written in C plus. *J. Appl. Crystallogr.* **2018,** 51, 210–218.

21. Thompson, P.; Cox, D.; Hastings, J. Rietveld refinement of Debye–Scherrer synchrotron X-ray data from Al_2O_3. *J. Appl. Crystallogr.* **1987,** 20, 79-83.

22. Young, R. A. The rietveld method. *International union of crystallography*: 1993.

23. Kresse, G.; Furthmüller, J. Efficient Iterative Schemes for Ab Initio Total-Energy Calculations Using a Plane-Wave Basis Set. *Phys. Rev. B* **1996,** 54, 11169-11186.

24. Perdew, J. P.; Burke, K.; Ernzerhof, M. Generalized Gradient Approximation Made Simple. *Phys. Rev. Lett.* **1996,** 77, 3865-3868.

25. Li, Y. C.; Yi, H. B.; Xu, J. G.; Kuang, X. J. High oxide ion conductivity in the Bi^{3+} doped melilite $LaSrGa_3O_7$. *J. Alloys Compd.* **2018,** 740, 143-147.

26. Hosono, H.; Kitano, M. Advances in materials and applications of inorganic electrides. *Chem. Rev.* **2021,** 121, 3121-3185.

27. Li, K.; Gong, Y.; Wang, J.; Hosono, H. Electron-Deficient-Type Electride Ca5Pb3: Extension of Electride Chemical Space. *J. Am. Chem. Soc.* **2021,** 143, 8821-8828.

28. Li, K.; Blatov, V. A.; Wang, J. Discovery of Electrides in Electron-Rich Non-Electride Materials via Energy Modification of Interstitial Electrons. *Adv. Funct. Mater.* **2022**, 2112198.

29. Dale, S. G.; Johnson, E. R. Theoretical Descriptors of Electrides. *J. Phys. Chem. A* **2018,** 122, 9370-9391.

30. Wu, J.; Li, J.; Gong, Y.; Kitano, M.; Inoshita, T.; Hosono, H. Intermetallic electride catalyst as a platform for ammonia synthesis. *Angew. Chem. Int. Edit.* **2019,** 58, 825-829.

31. Schutt., J.; Schultze, T. K.; Grieshammer, S. Oxygen Ion Migration and Conductivity in

$LaSrGa_3O_7$ Melilites from First Principles. *Chem. Mater.* **2020,** 32, 4442-4450.

32. Girifalco, L. A. Statistical mechanics of solids. *Oxford University Press*: 2003.

33. Li, Z.; Yang, J.; Hou, J. G.; Zhu, Q. Is mayenite without clathrated oxygen an inorganic electride? *Angew. Chem. Int. Edit.* **2004,** 43, 6479-6482.

34. Hayashi, K.; Sushko, P. V.; Hashimoto, Y.; Shluger, A. L.; Hosono, H. Hydride ions in oxide hosts hidden by hydroxide ions. *Nat. Commun.* **2014,** 5, 3515.

35. Irvine, J. T. S.; Sinclair, D. C.; West, A. R. Electroceramics: Characterization by Impedance Spectroscopy. *Adv. Mater.* **1990,** 2, 132-138.

36. Johnson, D. ZView: a software program for IES analysis, version 2.8. *Scribner Associates, Inc., Southern Pines, NC* **2002,** 200.

37. Raghvendra, S.; Singh, R. K. Electrical properties of Ba doped LSGM for electrolyte material of solid oxide fuel cells. *Solid State Phys.* **2013,** 1512, 976-977.

38. Wang, F.; Hu, E.; Wang, J.; Yu, L.; Hong, S.; Kim, J.-S.; Zhu, B. Tuning La_2O_3 to high ionic conductivity by Ni-doping. *Chem. Commun.* **2022,** 58, 4360-4363.

Table of Contents synopsis

The interstitial oxide ions located in the pentagonal rings of the non-stoichiometric $La_{1.5}Sr_{0.5}Ga_3O_{7.25}$ melilite oxide ion conductor may be removed and replaced by electron anions, which are confined within the pentagonal rings, and therefore convert the melilite interstitial oxide ion conductor into a zero-dimensional (0D) electride.